Climatology of SO2 and UV absorber at Venus' cloud top from SPICAV-UV nadir dataset

Emmanuel Marcq, Kandis Lea Jessup, Lucio Baggio, Therese Encrenaz, Yeon Joo Lee, Franck Montmessin, Denis Belyaev, Oleg Korablev, Jean-Loup Bertaux

Version of Record: https://www.sciencedirect.com/science/article/pii/S0019103519302283
Manuscript_b82b2ee71b7b948041db35e1f811545d

Climatology of SO_2 and UV absorber at Venus' cloud top from SPICAV-UV nadir dataset

Emmanuel Marcq[a,*], Kandis Lea Jessup[b], Lucio Baggio[a], Thérèse Encrenaz[c], Yeon Joo Lee[d], Franck Montmessin[a], Denis Belyaev[e], Oleg Korablev[e], Jean-Loup Bertaux[a,e]

[a] *LATMOS/CNRS/Sorbonne Université/UVSQ, 11 boulevard d'Alembert, F-78280 Guyancourt, France*
[b] *South West Research Institute, Boulder, CO, USA*
[c] *LESIA/CNRS/Observatoire de Paris, 5 place Jules Janssen, F-92195 Meudon, France*
[d] *University of Tokyo, Kashiwa, Japan*
[e] *Space Research Institute (IKI), Russian Academy of Sciences, Moscow 117997, Russia*

Abstract

Following our previous work (Marcq *et al.*, 2011, 2013), we have updated our forward radiative transfer code and processed the whole SPICAV-UV/Venus Express nadir dataset (2006-2014) in order to retrieve SO_2 abundance at cloud top – assuming a SO_2 decreasing scale height of 3 km and a ratio SO/SO_2 tied to 10% – as well as the imaginary index of scattering mode 1 particles, representative of the remaining UV absorption, since the OSSO vertical profile found by Frandsen *et al.* (2016) cannot account for our observations. Our main results mostly confirm and extend the validity of those discussed by Marcq *et al.* (2013), namely: (i) long-term variations of low latitude SO_2 at 70 km between $\sim$ 100 ppbv (2007, 2009) and less than 10 ppbv (2014); (ii) in average, decreasing SO_2 with increasing latitude and depletion near the sub-solar point, consistent with a competition between advection and

*E-mail: emmanuel.marcq@latmos.ipsl.fr

photo-chemical destruction; (iii) secular increase of mode 1 imaginary index at 250 nm, from 10^{-2} to $5 \cdot 10^{-2}$ between 2006 and 2010; (iv) if not related instead to long-term variability, a possible localized enrichment of SO_2 and UV brightness increase above the western slopes of Aphrodite Terra, consistent with Bertaux *et al.* (2016) supply mechanism through orographic gravity waves. This spatial and temporal variability underlines the need for a long term monitoring of Venus SO_2 and cloud top from ground-based facilities until the next generation of Venusian orbiters is operational.

Keywords:

Venus, atmosphere, Ultraviolet, observations, Atmospheres, composition

---

1. Introduction

Sulphur dioxide is arguably the most variable species in Venus' cloud top atmosphere, on a large range of temporal and spatial time scales. The first attempt to detect it in UV only yielded a 0.1 ppmv upper limit (Jenkins *et al.*, 1969). Yet, a decade later, Barker (1979) found between 0.1 and 0.5 ppmv of SO_2 using the same UV spectral range. The most extensive data set before *Venus Express* was acquired with UVIS onboard *Pioneer Venus* (Esposito *et al.*, 1979; Esposito, 1984; Esposito *et al.*, 1988), and revealed an important short term variability, as well as a long term decrease between 1978 and 1988. These long-term variations were interpreted as possible evidence for active volcanism, which would alter the thermal buoyancy of the lower atmosphere and allow for an intermittent resupply of SO_2 above Venus' clouds, where it is photochemically destroyed. Meanwhile, IR measurements from *Venera 15* (Zasova *et al.*, 1993) and UV measurements from rockets (Na *et al.*, 1994)

also evidenced a latitudinal gradient, with SO_2 increasing with increasing latitude, consistent with a photochemical control of SO_2 since photolysis is less effective at higher latitudes.

After a blank decade (1995-2005), Venus exploration (including cloud top SO_2 monitoring) resumed with ESA *Venus Express*. Occultation measurements from SOIR (Belyaev *et al.*, 2008) allowed for a retrieval of SO_2 scale height above the clouds, confirmed that SO_2 had returned to the relatively high values of the early 1980s, and evidenced a reversal in the latitudinal gradient of SO_2. These features were confirmed by our first SPICAV-UV nadir measurements (Marcq *et al.*, 2011, 2013), along with a long-term decrease of low latitude SO_2 similar to the one observed by *Pioneer Venus*. In parallel, high spectral resolution measurements in the thermal IR using NASA IRTF (Encrenaz *et al.*, 2012, 2016, 2019), or in the UV using STIS/HST (Jessup *et al.*, 2015) have confirmed and supported this trend, with two possible SO_2 regimes above the clouds: a high abundance regime more prevalent in the early 1980s or late 2000s, with a large number of SO_2 plumes located at lower latitudes and a negative latitudinal gradient, and a low abundance regime with little to no SO_2 convective plumes, and a reversed latitudinal gradient more typical of the early 1990s or mid-2010s. The transition between these regimes can occur within a few Earth days (Jessup *et al.*, 2015), and accounts for the large short-term dispersion of the measurements. The long-term change in the relative prevalence of these two regimes explain the long-term change in the average SO_2 latitudinal gradient that we observed in our previous study (Marcq *et al.*, 2013, Fig. 2). Nevertheless, the physical processes ruling both these regimes are still poorly known. Convective mix-

ing with the lower atmosphere where SO_2 is always abundant – more than 100 ppmv near 30-40 km (Bézard *et al.*, 1993; Marcq *et al.*, 2008; Arney *et al.*, 2014) is most certainly involved, but the reasons behind these variations of the convective mixing intensity are still debated, including possible episodic volcanism or other atmospheric processes.

Following the recent progress in our knowledge of Venus clouds and hazes (Luginin *et al.*, 2016), as well as in our processing of SPICAV-UV nadir spectra, we have completely rewritten our analysis pipeline and processed the whole of SPICAV-UV archive in order to complete and update our SO_2 climatology, as well as other derived observable parameters such as the mean UV brightness of the clouds. A short description of our data set in given in §2, and of our forward radiative transfer model in §3, since both were already extensively described in a previous paper (Marcq *et al.*, 2019). Our results about SO_2 and UV absorber variability is detailed in §4 and their scientific implications further commented in §5, before we summarize and conclude in §6.

2. Observations

Our data set and processing is detailed in our previous paper (Marcq *et al.*, 2019). For the convenience of the reader, we summarize the main points below.

2.1. Data set

Our data set consists in the whole archive of SPICAV-UV (Bertaux *et al.*, 2007) nadir or near-nadir spectra, from 170 to 320 nm at a spectral resolution

of 1 nm. There are 1508 such observations, from 2006-06-01 up to 2014-11-20. Coverage in local time and latitude is extensive except for the south polar region (Marcq *et al.*, 2019, their Fig. 1), with southern hemisphere observations dominated by ~~near nadir *tracking*~~ *pointing* *mode* observations over single ~~spots~~spot targets (implying continuously changing emission and phase angles along the orbit), whereas northern hemisphere observations consisted mainly ~~in nadir~~ *latitudinal scans* (where emission angle is essentially zero along the orbbital track).

2.2. Processing

The first steps of data processing are unchanged since Marcq *et al.* (2011), namely cosmic ray hit removal, dark subtraction, correction of electronic readout artifact, flat-fielding, wavelength assignment. Most recent progress come from a better knowledge of the instrument ~~PSF~~Point Spread Function (PSF), especially at large distances from the center (far wings). Richardson-Lucy deconvolution is now performed in order to clean the far wing contribution, which enables the scientific use of spectra from 200 nm instead of 215 nm in our first analyses, which in turn enables to retrieve more observable parameters relative to Venus' clouds and SO_2.

Photometric calibration of the spectral radiance spectra was performed from the CALSPEC catalog of bright UV stars observed in-flight (Bohlin *et al.*, 2014). From these calibrated spectral radiances, we computed the corresponding radiance factors $\beta(\lambda) = \frac{I(\lambda) \times \pi \text{ sr}}{F_\odot(\lambda)}$ where $I(\lambda)$ is the spectral radiance and $F_\odot(\lambda)$ a reference top-of-atmosphere solar spectral irradiance. These solar spectral irradiance were extracted from the SOLSTICE II database (McClintock *et al.*, 2005) at the corresponding date to account for the solar

cycle variations. We also corrected a spectral feature in these solar spectra near 230-240 nm that our forward radiative transfer model was unable to reproduce, no matter the prescribed values of the atmospheric parameters.

3. Forward Model

3.1. Overview

A detailed description of the forward radiative transfer we use is available in Marcq *et al.* (2019). For the sake of convenience, we present below a summary of its features and free parameters. The radiative transfer equation solver we use is the pseudo-spherical version of DISORT (Dahlback and Stamnes, 1991) using 16 streams.

3.1.1. Aerosols

The model encompasses the 50-110 km altitude range. We consider a bimodal log-normal size distribution ($r_{\text{eff}} = 0.12$ and 0.8 µm respectively, with an effective dimensionless variance of $\nu_{\text{eff}} = 0.15$) of aerosol particles following Luginin *et al.* (2016).

The vertical profiles for both modes that we consider are ~~simplified from the same reference (Luginin *et al.*, 2016)~~ a simplification from the retrieved profiles derived by Luginin *et al.* (2016) and can be seen in Fig. 1. ~~Number density is capped for both particles at in the lower part the model (respectively $2 \cdot 10^8$ and 10^8 particles/m^3 for mode 1 and mode~~ Above a altitude named Z_2 hereafter, mode 2 ~~), and the number density ratio $n_1/n_2 = 1000$ is fixed in the upper~~ particle number density decreases following $n_2(z > Z_2) = 10^8 \exp\left(\frac{Z_2 - z}{4.5\ \text{km}}\right)$ particles/m^3. Below this altitude, we have a constant, capped value $n_2(z < Z_2) = 10^8)$ particles/m^3.

Figure 1: Synthetic number density profiles for both particle modes. Z_2 is a free parameter in our model, which captures cloud top altitude variations.

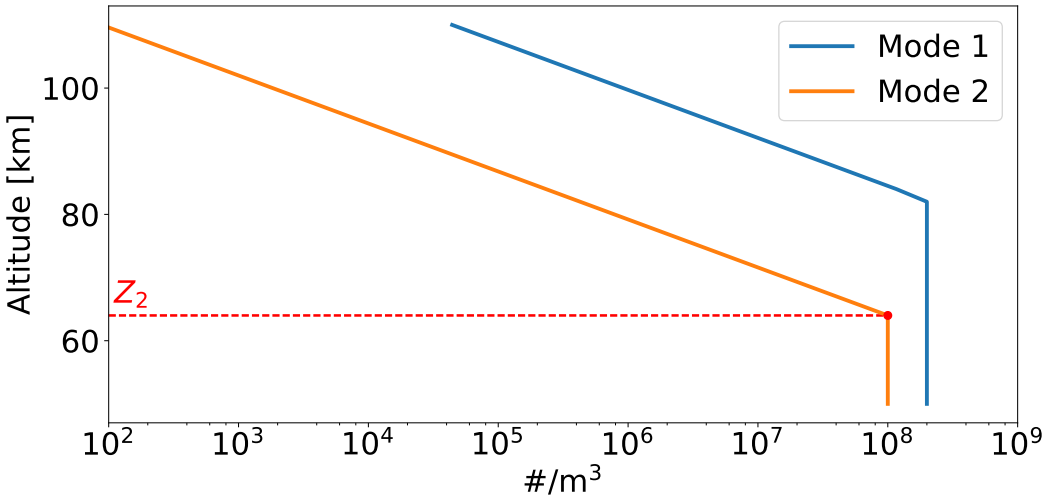

Mode 1 particles follow a similar profile, with a constant ratio $n_1/n_2 = 1000$ in the upper part of the model, and a cap at $2 \cdot 10^8$ particles/m^3 in the lower part of the model. ~~The altitude~~ Z_2 ~~above which mode 2 particles decrease following a scale height of 4.5 km~~ is a free parameter in our model, ~~representative of~~ which is related to the cloud top altitude ~~variations — we find that~~ $Z_{\mathrm{TOP}}(250\ \mathrm{nm})$, classically defined (Titov *et al.*, 2018) as the altitude where nadir optical depth is equal to one (consdering only particulate opacity). Numerical intergration yields $Z_{\mathrm{TOP}}(250\ \mathrm{nm}) = Z_2 + 4.95$ km for the above described extinction profiles.

The real refractive index of both modes is taken from Hummel *et al.* (1988) for a 75%-25% H_2SO_4-H_2O mixture. Imaginary indices for both modes are discussed in §3.2, the imaginary index of mode 1 particles at 250 nm~~being a~~, $m_i(250\ \mathrm{nm})$, being another free parameter.

3.1.2. Gaseous Species

The gaseous species involved in absorption and/or scattering are displayed in Fig. 2. CO_2 Rayleigh and absorption cross-section is unchanged since Marcq *et al.* (2013). SO_2 and SO cross-sections were compiled from various sources by Jessup *et al.* (2015), and we use the same. New gaseous species that we consider is O_3 and OCS, whose UV absorption cross-sections are taken from Sander *et al.* (2011).

CO_2 vertical profile is computed from hydrostatic equilibrium assuming VIRA-2 temperature profile (Moroz and Zasova, 1997). Following recent intercomparison between observations and models (Vandaele *et al.*, 2017a; Marcq *et al.*, 2018), we consider that SO_2 vertical profile is capped at 150 ppmv in the lower part of the model, and decreases according to a scale height of 3 km in the upper part of the model. Its mixing ratio at 70 km is a free parameter of our model. Since we cannot distinguish individual SO and SO_2 absorption lines at SPICAV-UV spectral resolution, we have to assume that SO vertical profile is tied ~~at~~ to 10% of SO_2, according to the average values dervied from higher spectral resolution HST/STIS measurements (Jessup *et al.*, 2015). OCS vertical profile is taken from Haus *et al.* (2015), and O_3 is considered uniformly mixed between 55 and 70 km. Its mixing ratio in this range is an optional free parameter of the model.

O_3 measurements is the main topic addressed by Marcq *et al.* (2019). O_3 absorption is considered only when including it yields a substantial reduction in the reduced χ^2 (namely, 5.5). We adopt the same criterion in the present study. Example of a fitted spectrum with and without O_3 can be found in ~~Marcq *et al.* (2019, their Fig. 2)~~Marcq *et al.* (2019, their Fig. 3).

Figure 2: UV cross-sections of considered gaseous species

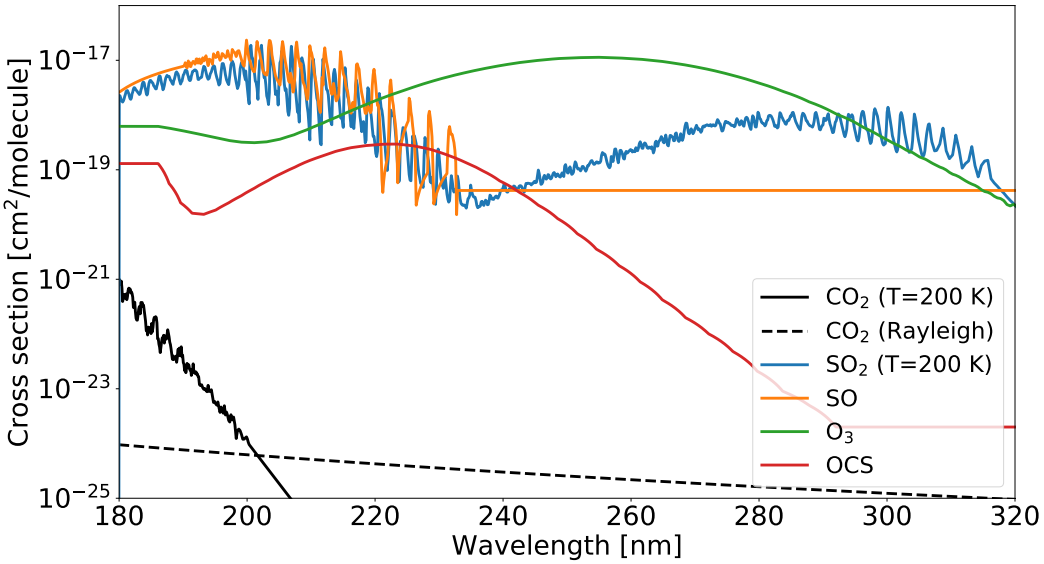

3.2. Model Sensitivity

The modeled effect of varying SO_2 (Fig. 3) is easy to understand: since SO_2 has two broad electronic absorption bands peaking near 215 and 280 nm, respectively, these two absorption bands have a relative depth that becomes more pronounced with increasing SO_2 abundance. However, it is noteworthy that the SO_2 influence extends throughout the whole spectrum, even though the cross-section is a continuum between 240 and 270; nm reaching a local minimum near 240 nm. Sensitivity of the inferred radiance factor to SO_2 absorption in the 240-270 nm region is a telltale sign that multiple scattering is prevalent, so that most backscattered photons have traveled through long enough optical paths into deep, SO_2-rich atmospheric layers that its smaller absorption cross-section is partially offset. This is important when considering SO_2 measurement proxies such as image ratios between 280 and 240 nm:

Figure 3: Synthetic radiance factors for a cloud top altitude of 74 km, $m_i(250\text{ nm}) = 10^{-2}$ and varying SO_2 abundances. The considered geometry is pure nadir viewing, with a solar zenith angle of 30°.

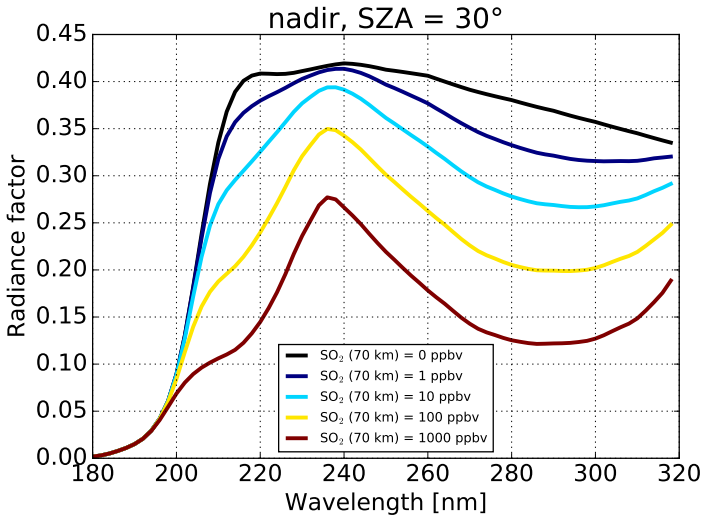

the image at 240 nm, though not dominated by SO_2 ~~gaz~~ gas absorption, is also not independent from the spatial SO_2 variations.

At Venus' cloud top, the observed SO_2 absorption band is primarily related to the column density above the cloud top (Marcq *et al.*, 2011, 2013). Thus, altering the cloud top altitude results in a change in the total SO_2 column density above the cloud top, according to the assumed vertical profile of SO_2 number density. The primary effects of altering the cloud top altitude while making no change to SO_2 vertical profile would therefore be very similar to the results displayed in Fig. 3, because the direct outcome of the change in the cloud top altitude is a change in the SO_2 column density above that altitude. However, as Fig. 4 shows, changing the cloud top altitude will impact the total absorption occuring in the two SO_2 electronic absorption

Figure 4: Synthetic radiance factors for $m_i(250\text{ nm}) = 10^{-2}$, and varying SO_2 abundances as well as cloud top altitudes ~~et~~ at 250 nm. The considered geometry is pure nadir viewing, with a solar zenith angle of 30°.

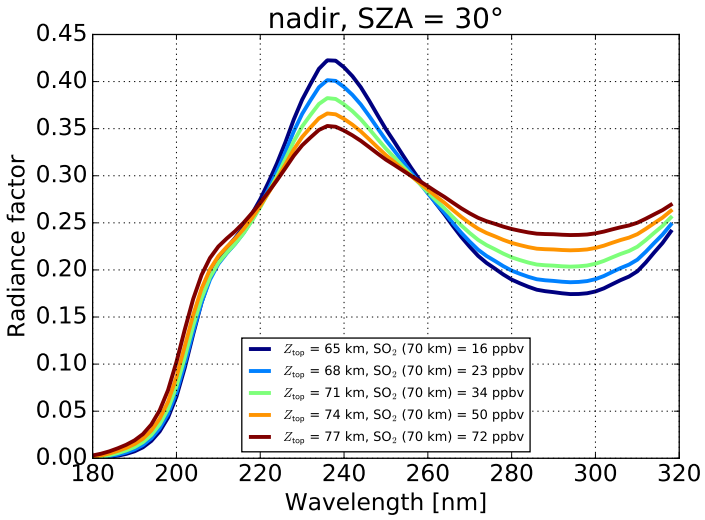

bands differently, because the 280 nm band has a lower cross-section than the 215 nm band. Thus, for example, increasing the cloud top altitude results in a lower relative depth for the 280 nm SO_2 absorption band compared to the 215 nm band. Similarly, the lower cross-section of the 280 nm band allows that band to probe deeper into the atmosphere than the 215 nm band. Notably, at lower altitudes both Rayleigh scattering and CO_2 absorption are stronger.

Altering the imaginary part m_i of the refractive index of mode 1 particles yields the expected outcome, namely lowering the albedo when particles are darker (Fig. 5). However, altering the spectral slope of this mode 1 absorption results in a spectral distortion very much alike that of changing the cloud top altitude. This resulted in a fitting degeneracy ~~when~~ if we

tried to fit both the mode-1 absorption spectral slope and cloud top altitude together. We therefore chose to keep only the cloud top altitude as a fitted parameter, and adopted a ~~spectral dependency~~ fixed spectral slope for $m_i(\lambda) = m_i(250\text{ nm}) \times \exp\left(\frac{\lambda - 250\text{ nm}}{40\text{ nm}}\right)$ ~~where the exponential function~~ , fitting only $m_i(250\text{ nm})$. The 40 nm slope accounts for the decreasing mode 1 single-scattering albedo with increasing wavelength. Using this ~~relationship~~fixed 40 nm value, our low latitude cloud top average altitude near 250 nm was then in agreement with the most recent IR measurements (Ignatiev *et al.*, 2009) that do not suffer from this degeneracy. ~~The~~ This 40 nm value is slightly less steep than our previous estimate of about 34 nm (Marcq *et al.*, 2011), which can be explained by our updates to the spectral calibration of radiance factors (Marcq *et al.*, 2019). At first, we assumed that this dependency applied to both particle modes, but this assumption resulted in spurious correlations between effective airmass and cloud top altitude as well as imaginary refractive index retrievals – mode 2 particles contribute more to backscattering at smaller airmass since they dominate at lower altitudes. Empirically, we found that assuming a constant, fixed imaginary refractive index of 10^{-3} for mode 2 particles minimized such spurious correlations.

Since this fixed value is much larger than the imaginary refractive index of pure H_2SO_4-H_2O solutions in this wavelength range, this may be indicative of two different UV absorbers: one, well mixed with mode 2 and mode 1 particles and with little spectral dependency between 200 and 300 nm, and the other one, mixed with mode 1 particles only and horizontally variable, absorbing more towards longer wavelengths. This latter absorber is likely the same absorber than the infamous near UV-blue absorber peaking

Figure 5: Synthetic radiance factors for a cloud top altitude of 74 km, SO_2 volume mixing ratio of 50 ppbv at 70 km and varying m_i(250 nm). The considered geometry is pure nadir viewing, with a solar zenith angle of 30°.

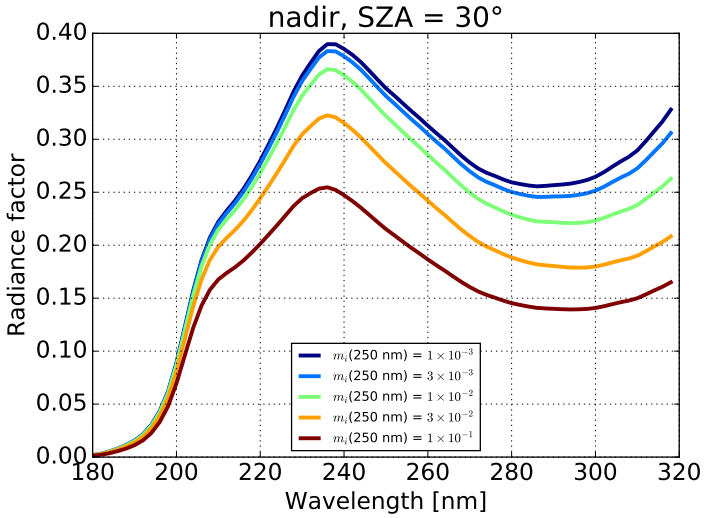

near 365 nm, our retrieved imaginary indexes in the 10^{-2}-10^{-1} range and spectral slope being in agreement with recent determinations of this imaginary refractive index over a larger spectral range extending to the visible range (Pérez-Hoyos *et al.*, 2018).

We will further discuss the scientific implications in §5.1.

4. Results

4.1. Retrieval uncertainties

The above described forward model is then compared to 30-s binned SPICAV-UV observations through a Levenberg-Marquardt iterative algorithm (Newville *et al.*, 201 . Three parameters are always fitted, namely: SO_2 mixing ratio at 70 km, Z_2 and m_i(250 nm). O_3 mixing ratio is also fitted when its inclusion results

in a significant reduction in residual χ^2 – the interested reader should refer to Marcq *et al.* (2019) for further details about O_3 in the SPICAV-UV nadir data set.

The Levenberg-Marquardt algorithm yields a covariance matrix, from which $1 \cdot \sigma$ statistical uncertainties are derived for each fit, along with the residual reduced χ^2. The median reduced χ^2 of the whole dataset is 16.6 (which indicates that systematic errors do exist, and/or that the observatoinal uncertainity may be underestimated). Hereafter, we only consider our fits valid if their χ^2 is less than 3 times this median value ($\chi^2 < 50$).

In this valid dataset, the median relative $1 \cdot \sigma$ uncertainty on SO_2 retrievals is 38%, substantially less than the 3-order of magnitude spatial and temporal variability of SO_2 (§4.2, §4.3.1): the lowest $3 \cdot \sigma$ detection of SO_2 is about 0.6 ppb, and the highest values on the order of 1000 ppbv. Similarly, the median relative $1 \cdot \sigma$ uncertainty on m_i retrievals is 25%, also substantially less than its spatial and temporal variability (§4.2, §4.3.2). Finally, the median relative uncertainty on our cloud top altitude retrievals is on the order of 1 km.

4.2. Temporal variability

The long term evolution over the whole extent of *Venus Express* of our retrieved cloud top SO_2 and imaginary index of mode 1 particles are shown respectively on Fig. 6 and 7. ~~We restricted the analysis of~~ Since most SO_2 ~~temporal variability to lower latitudes only so that we do not encompass any bias in latitude , since SO_2 and latitude are correlated in our data set~~ content is actually located below $\pm 20°$ in latitude (see §4.3), we will discuss hereafter the temporal variabilty of SO_2 temporal variability only in this low-latitude

bin. The most striking features in both retrieved parameters are: (i) short-term dispersion is much larger than retrieval uncertainties, and spans two orders of magnitude for SO_2 and one for the imaginary index; (ii) despite this short-term variability, longer term trends can be observed.

For SO_2, the overall trend consists in an overall decline by a factor 5 to 10 from 2007 (about ~~80 ppbv)~~ 80 ppbv in median) to 2014 (about 10 ppbv). This steady decline is not monotonous though: after the peak in 2007, surges in SO_2 can observed in 2009, 2012, and late 2013. This trend is consistent with our previous findings for 2006-2012 (Marcq *et al.*, 2013), except for the 2009 peak that was not noticed at the time, probably due to an insufficient number of analyzed observations compared to our extensive analysis presented here. ~~Comparison with~~ STIS/HST retrievals (Jessup *et al.*, 2015) and ~~with~~ TEXES retrievals (Encrenaz *et al.*, 2012, 2016), extrapolated at 70 km assuming a scale height of 3 km~~is excellent, and~~ , are fully consistent with the statistical dispersion of SPICAV-UV retrievals, which highlights the fact that these "snapshot" observations are actually representative of the ~~median state of~~ cloud top SO_2 as observed ~~statistically~~ by SPICAV. More generally, these variations are in agreement with the inter-comparison of available SO_2 measurements detailed by Vandaele *et al.* (2017b), as well as recent UVI/Akatsuki results (Lee *et al.*, 2017).

Regarding UV darkness (as measured through mode 1 imaginary index at 250 nm), the long term trend can be divided in two time periods: first a 5-fold increase from 2006 ($\sim 10^{-2}$) until 2010 ($\sim 5 \cdot 10^{-2}$), and then a constant, darker plateau from 2011 onward until the end of the mission in late 2014. These variations are most pronounced at lower and mid-latitudes, latitudes

Figure 6: Temporal evolution of SO_2 mixing ratio at 70 km for latitudes lower than 30°. The red line stands for the moving median value, and white diamonds~~are TEXES~~ /squares show other SO_2 ~~mixing ratios from Encrenaz *et al.* (2016)~~measurements in the same time interval.

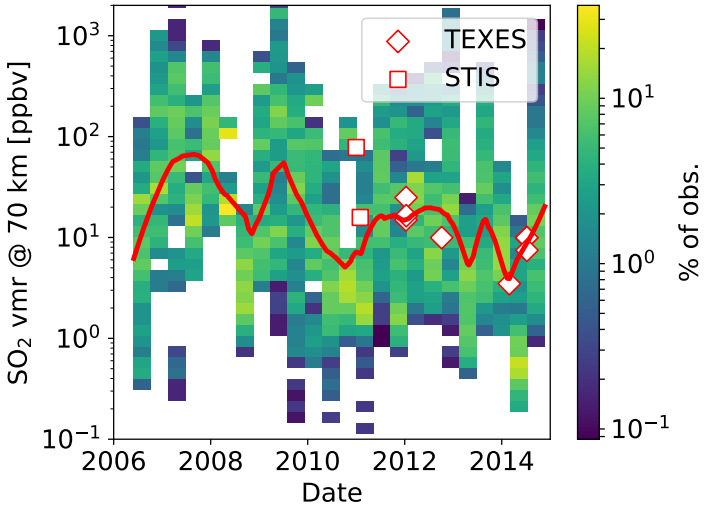

above 60° seem less affected by this trend. Here also, these results compare well with our previous results (Marcq *et al.*, 2013) where we accounted for this UV darkening through a fitted scaling factor, but also with the 40% UV albedo darkening observed in 2006-2011 by *Venus Express*/VMC at 365 nm (Lee *et al.*, 2015). This agreement between two diffrent instruments (VMC and SPICAV) and the fact that the albedo latitude variation trends inferred from either the VMC and SPICAV data sets are consistent, even though the binning and the reduction of the two data sets ~~is~~ are unique lead us to believe that this darkening is genuine, and not an artifact from the aging of the SPICAV UV detector.

Figure 7: Temporal evolution of mode 1 imaginary refractive index at 250 nm. The red line stands for the moving median value. Absolute latitude is color-coded.

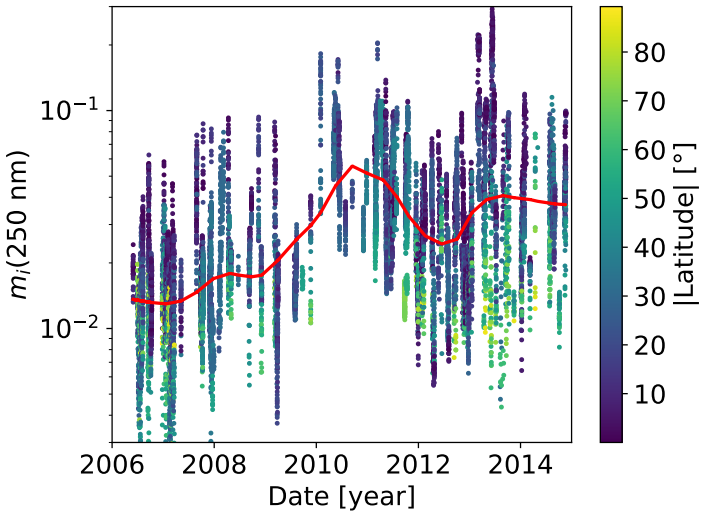

4.2.1. SO_2 periodogram

The SO_2 variations observed in Fig. 6 suggest they may exhibit some periodicity. In order to discuss them more quantitatively, we computed a Lomb-Scargle periodogram of both SO_2 mixing ratio as well as its logarithm (since we present all of our SO_2 results in a logarithmic scale). Lomb-Scargle periodograms are well suited when the temporal sampling of measurements is uneven (as it is the case here), but may exhibit "ghost" harmonics for integer multiple values of the genuine frequency.

These periodograms are shown in Fig. 8. Assuming that genuine frequencies would show up in both SO_2 and $\log(SO_2)$ periodograms, we find that our frequency signal is dominated by a 400 Earth day period (and its ghost harmonics near 200, 135 and 100 days) component, that can be seen between the SO_2 surges in Fig. 6. A 110-day long component is also visible,

Figure 8: Lomb-Scargle periodogram of low-latitude SO_2 in log and linear scales. Periods discussed in the main text are shown in dashed, with the 400-day period and its ghost harmonics shown in dashed black.

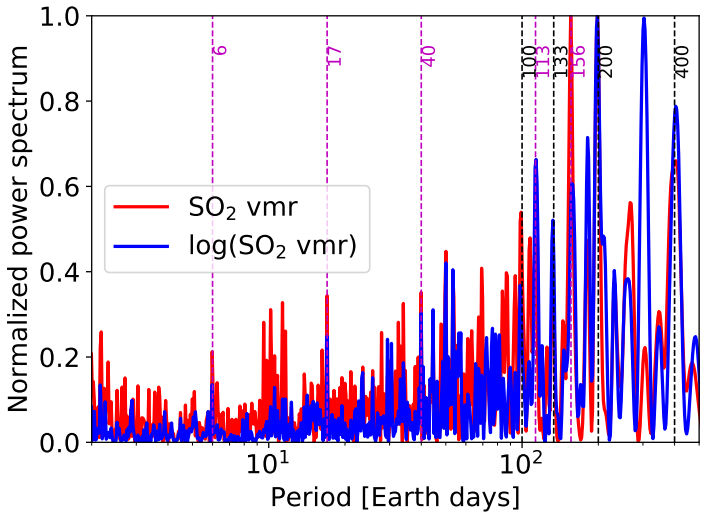

close to the solar day on Venus surface, suggesting a link between SO_2 variations and local solar time at the surface reminiscent of the similar period seen by Bertaux *et al.* (2016) for the UV brightness as observed by VMC. We present the correlation between topography and SO_2 in more detail in §4.3.1.

Other possible periods that are significantly above noise include a 155 Earth day component, as well as medium term components (40, 17 and 6 Earth days). Noticeably, a 4-day period is absent, implying that SO_2 patches are shorter lived than the super-rotation period at cloud top.

4.3. Spatial variability

4.3.1. SO_2

The binned latitudinal distribution of our SO_2 retrievals is shown in Fig. 9. The main features from our previous analyses (Marcq *et al.*, 2013, 2011) are still valid, namely: (i) there is a large dispersion, spanning more than two orders of magnitude at lower latitudes and about one order of magnitude at higher latitudes (ii) the median SO_2 value is larger at lower latitudes (typically 5 to 100 ppbv, median 20 ppbv below 30°), due to the occurrence of SO_2 "plumes" (above 100 ppbv) that do not occur at higher latitudes. The observed latitudinal pattern remains consistent with the SO_2 gas distribution being dominantly controlled by a Hadley-cell type circulation as reported previously (Jessup and Mills, 2019; Vandaele *et al.*, 2017b; Jessup *et al.*, 2015; Marcq *et al.*, 2013, 2011) – thus is linked to large-scale (or deep) convective mixing process. The broad range of SO_2 abundance values observed at each latitude points to the perpetual competition between general circulation and the LST dependent photochemical destruction of SO_2 (Marcq *et al.*, 2013) which may produce order of magnitude changes in the cloud top abundances on a time scale of several Earth days (corresponding to 1-2 hours of LST considering the zonal super-rotation at cloud top) particularly at low latitudes. The SPICAV-observed variability patterns are fully consistent with other measurements in UV from HST/STIS (Jessup *et al.*, 2015) or in IR with IRTF/TEXES (Encrenaz *et al.*, 2012, 2016).

Our comprehensive data set also allows us to study the variability of SO_2 with respect to local solar time as shown in Fig. 10. A local minimum near noon (between 10am and 2pm) is evidenced. Interestingly, TEXES

Figure 9: SO_2 mixing ratio at 70 km with respect to latitude for all LSt values. The red line stands for the ~~moving~~ 10°-moving boxcar median value, and red error bars for the $1 \cdot \sigma$ statistical dispersion.

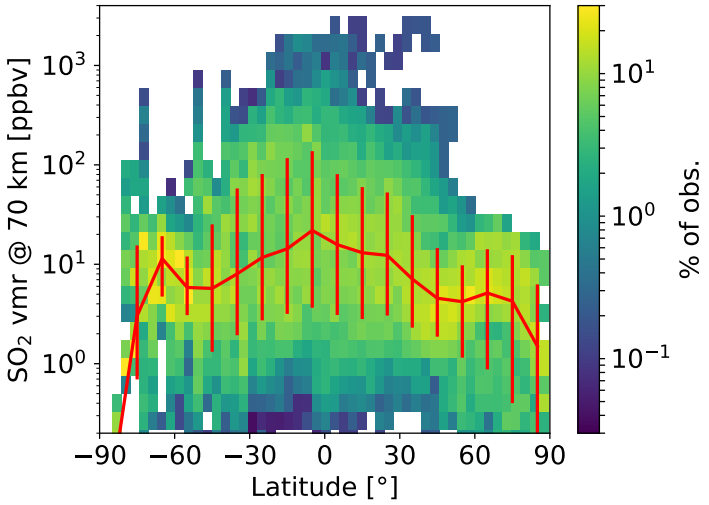

measurements also confirm the inefficiency of upwelling SO_2 plumes in the 10h to 14h local time interval (Encrenaz *et al.*, 2019). We further discuss the SO_2 and overall UV brightness variations with respect to local solar time in §5.2.

The SO_2 periodgram (§4.2.1) suggest that SO_2 and surface topography may be correlated. Therefore, we have mapped our SO_2 retrievals with respect to latitude and geographic longitude in Fig. 11. Besides the latitudinal trend already discussed, we notice a possible SO_2 enhancement located downwind of the western edge of the large equatorial high-altitude plateau known as *Aphrodite Terra* in the 30°-45° range. Similarly, the SO_2 volume mixing ratio observed by HST at low latitudes in the 0°-45°E longitude range was an order of magnitude higher than directly over *Aphrodite Terra* (Jessup and

Figure 10: SO_2 mixing ratio at 70 km for latitudes below 20° with respect to local solar time. The red line stands for the 1-hour moving boxcar median value, and red error bars for the $1 \cdot \sigma$ statistical dispersion.

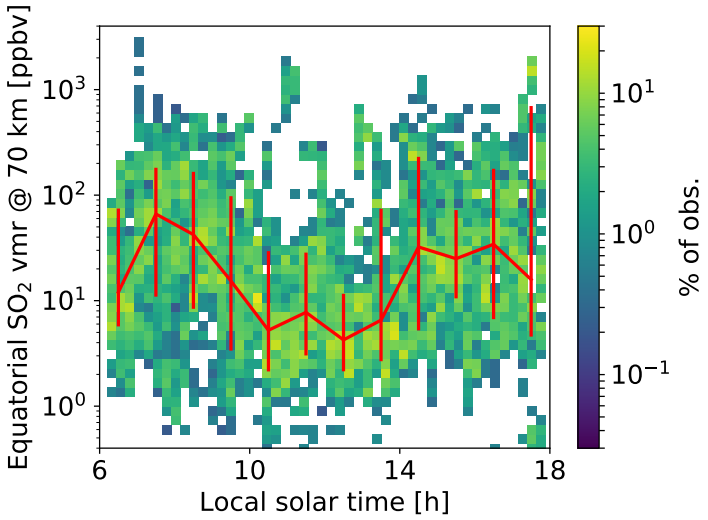

Mills, 2019). Yet TEXES measurements also displayed on Fig. 11 fail to report such an increase of SO_2 over the same ground location. Although the 70 km values inferred from TEXES data do not match the statistical averaged SPICAV values, a trend of increased SO_2 plumes at 0°-30°E vs. 60°-140°E is distinctly evident in the TEXES data (Encrenaz *et al.*, 2019, their Fig. 8). One should also note that the polar orbit of *Venus Express* implies that diffrent longitudes were observed at different dates, so that longitudinal and temporal variablity cannot be retrieved separately from these maps.

4.3.2. UV brightness

We have also investigated the correlation between topography and the retrieved absorption of mode 1 particles shown in Fig. 12 to determine if

Figure 11: Map (latitude vs. longitude) of SO_2 mixing ratio at 70 km. The contour lines follow topographic elevation – *Aphrodite Terre* is peaking near 90°E-0°. Crossed hatching indicated lack of meaningful data. Red diamonds show co-located day side TEXES retrievals, with red crosses showing the TEXES observations footprint.

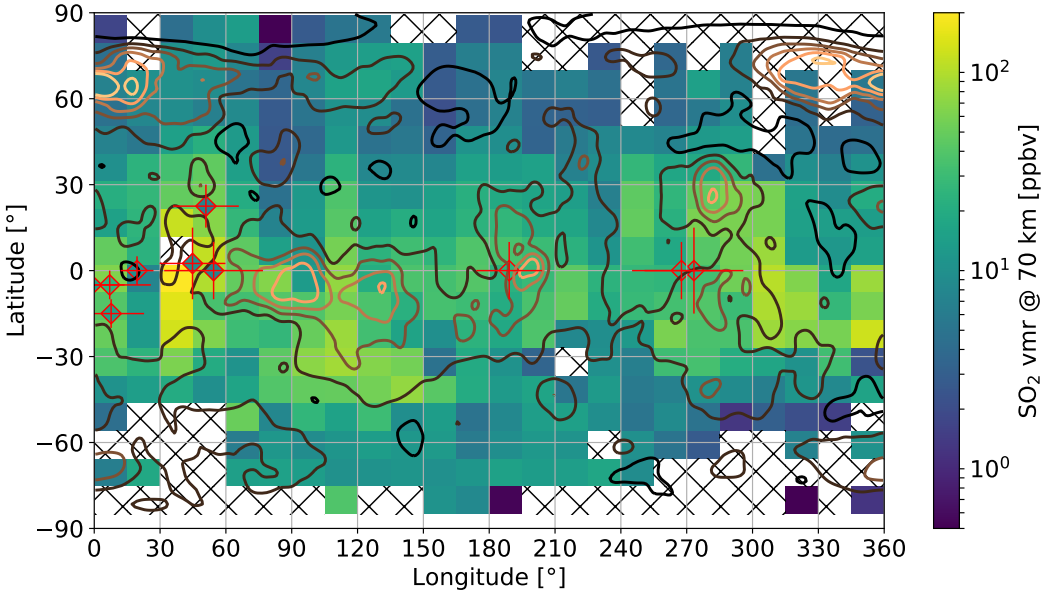

relationships between the albedo and the underlying topography proposed by Bertaux *et al.* (2016) are supported by our data, and to determine how the observed albedo trends might relate to the retrieved SO_2 abundances. We are able to do so, since the retrieved values of m_i(250 nm) exhibit an anti-correlation with the UV brightness of the cloud top (once SO_2 absorption is taken into account). Comparison of Figures 11 and 12 highlights that directly over *Aphrodite Terra* (60°-140°E, 15°S) where relatively SO_2 VMRs have been retrieved, the m_i values are low, suggesting a bright cloud top – this results confirms that the cloud top is brighter over Aphrodite but the anti-correlation between the cloud top albedo and the SO_2 gas abundance does not support that the abundance of both components (SO_2 and UV absorber) is controlled solely by linked vertical transport process (see §5).

Fig. ~~11~~ 12 also indicates that high m_i values are retrieved at lower latitudes, which is expected since convective activity is strongest at these latitudes due to the enhanced solar heating (Peralta *et al.*, 2007; Titov *et al.*, 2008, 2012). However, strong longitudinal variability in the cloud top brightness is observed within the low latitude region sampled by SPICAV; and the inferred brightness distribution is not symmetric with respect to the equator. Additionally, as already mentioned, the polar orbit of *Venus Express* leads to an uneven longitudinal sampling with respect to observation date, so that the observed distribution pattern may also be linked to long-term temporal variability.

In terms of local time and latitudinal variability, Fig. 13 shows that (i) UV brightness increases with increasing latitude, reaching a high plateau near 60°N; and (ii) UV brightness is lower between 10:00 and 16:00 at lower

Figure 12: Map (latitude vs. longitude) of mode 1 imaginary refractive index at 250 nm. The contour lines follow topographic elevation – *Aphrodite Terre* is peaking near 90°E-0°. Crossed hatching indicates lack of meaningful data.

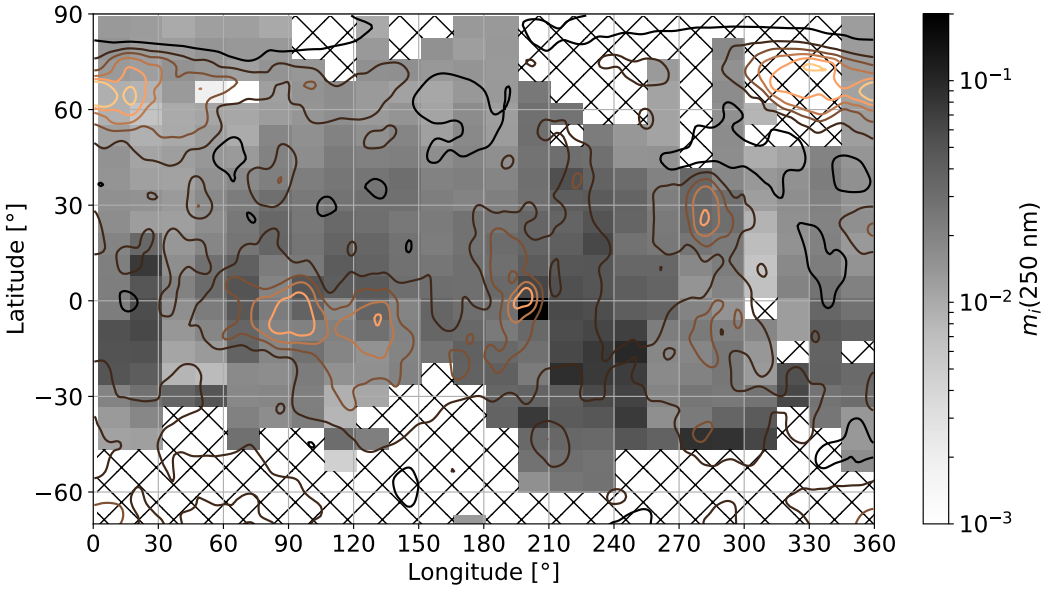

Figure 13: Pseudo-map (latitude vs. local solar time) of mode 1 imaginary refractive index at 250 nm. Hatched areas indicate lack of meaningful data

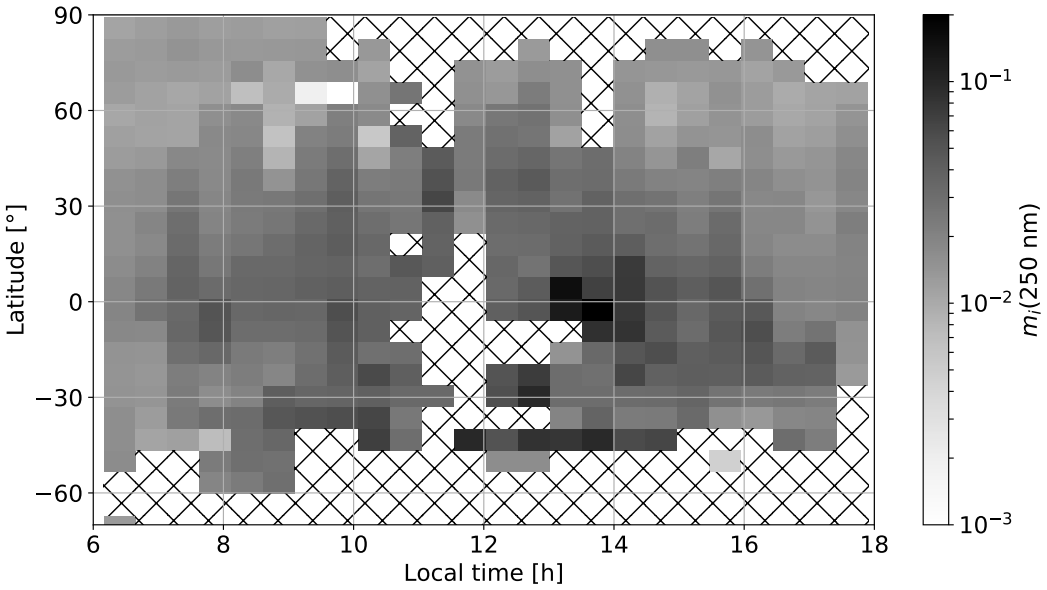

latitudes (below 30°). Both these patterns in latitude and local solar time are already known from previous studies (Titov *et al.*, 2008, 2012; Lee *et al.*, 2015). These already known trends, plus the fact that minimum UV brightness ~~(correlated with maximum m_i values)~~ is reached near 14:00 and not exactly at noon lead us to discard a spurious correlation of our retrievals with respect to airmass, which may occur if the assumed extinction vertical profiles are not representative of the real ones.

4.3.3. Cloud top altitude

Variations of cloud top altitude with respect to latitudes are shown in Fig. 14. The average low latitude cloud top altitude (defined as $\tau(250\ \text{nm}) = 1$ nadir level) we find is 73 ± 2 km in good agreement with already known

values (Ignatiev *et al.*, 2009; Pérez-Hoyos *et al.*, 2018). This is not surprising, since we adjusted the spectral slope of the UV absorber precisely to match this mean value (see §3.2). The already known decrease of cloud top altitude towards higher latitudes (Ignatiev *et al.*, 2009) is also observed, although the amplitude – about 10 km from equator to pole here instead of about 3 km according to Ignatiev *et al.* (2009) – is somewhat larger, and starts at lower latitudes (30° instead of 50°). Nevertheless, due to the aforementioned degeneracy between the spectral slope and cloud top altitude, reaching a qualitative agreement for this poorly constrained parameter retrieval is satisfactory, considering the need to keep as few free fitted parameters as possible in our forward model. Please note that simultaneous and co-loacted IR cloud top measurements would remove such a degeneracy, and allow for a detailed investigation of the spatial and temporal variability of the aerosol spectral slope.

5. Discussion

5.1. UV absorption

5.1.1. Nature of UV absorber

As already mentioned in §3.2, we suspect that our retrievals of the imaginary refractive index of mode 1 particles is directly related to the local abundance of the infamous UV absorber. Unfortunately, the only ~~spectropscopic~~ spectroscopic constraint we were able to derive is the spectral slope-related parameter of 40 nm. Such ~~an~~ a decrease of UV single scattering albedo with increasing wavelength in the SPICAV UV range is compatible with a large number of candidates for the UV absorber, including the most recent mix-

Figure 14: Cloud top altitude with respect to latitude. The red line stands for the 10° binned moving boxcar median value, and red error bars for the $1 \cdot \sigma$ statistical dispersion.

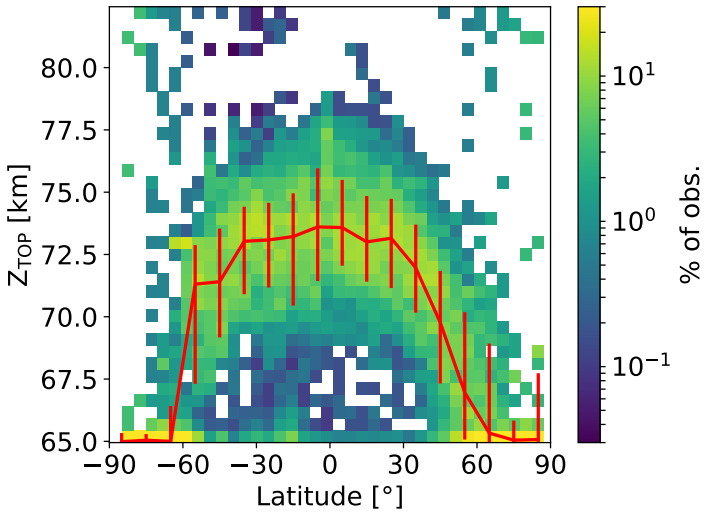

ture of cis- and trans-OSSO suggested by Frandsen *et al.* (2016). Actually, we first tried to fit the average UV brightness not through the refractive index of mode 1 particles, but with peak OSSO concentration following the theoretical vertical profile given by Frandsen *et al.* (2016) peaking near 62 km. It appeared then that we could not reach a satisfactory fit, the amount of OSSO required to match the mean albedo was at up to two orders of magnitude larger than the peak abundance given reported by Frandsen *et al.* (2016, about 10 ppbv), and in such a case suppressed all other gaseous spectral signatures (SO_2, SO, O_3) except for CO_2. So, if the unknown UV absorber were indeed OSSO, its vertical abundance profile and abundance would differ significantly from the theoretical values given by Frandsen *et al.* (2016).

Figure 15: Scatter plot between imaginary index of mode 1 particles at 250 nm and SO_2 mixing ratio at 70 km

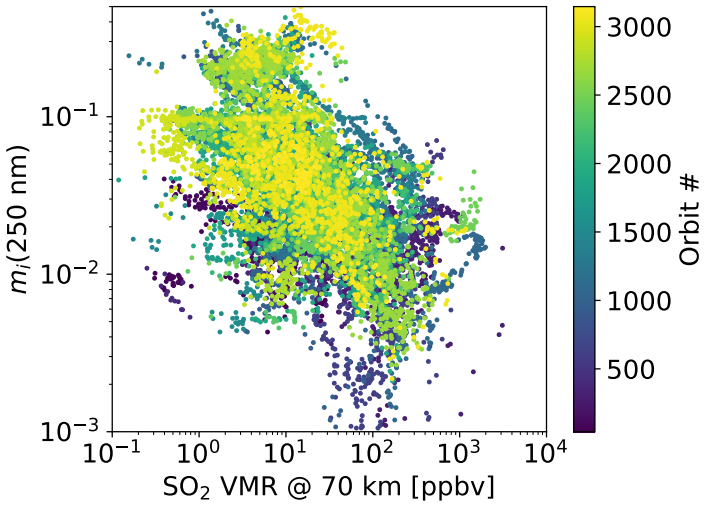

5.1.2. Correlation with SO_2

We already reported (§4.3) that low SO_2 abundances were observed within 2 hours of the subsolar point, and similarly the lowest UV brightness (minimum absorber abundance) was detected in the afternoon hours. The long-term trends are opposite too, with an observed secular decrease for SO_2, and secular increase of the UV absorption, see §4.2). This points to an anti-correlation between SO_2 and UV absorption that is confirmed in Fig. 15: although the statistical dispersion for both SO_2 and the imaginary refractive index m_i(250 nm) is large, there is an average decrease of one order magnitude for m_i relative to an increase of SO_2 of two orders of magnitude.

Such an anti-correlation using VMC 365 nm observations with respect to our previous estimates of SO_2 (Marcq *et al.*, 2013) was reported by Lee *et al.* (2015), as well as using high spectral resolution (line-resolving) retrievals of

SO_2 and SO with HST/STIS from Jessup *et al.* (2015). Therefore, we can safely dismiss that correlation would be a spurious artifact due to parasitic trends in the photometric calibration of SPICAV-UV spectra. There are two possible, non-mutually exclusive physical explanations already reported (Esposito, 1984; Jessup *et al.*, 2015) and supported by this study: (i) injections of SO_2 and H_2O from the deep atmosphere lead to an increased formation rate of uncontaminated H_2SO_4, UV-bright haze particles above the UV absorber; and (ii) on longer time scales, SO_2 is a precursor species to the UV absorber, so that there is a possible conversion of SO_2 into a sulfur-bearing UV absorber – SO_2 and the UV absorber being competing reservoirs of sulfur in such a case.

5.1.3. Comparison with VMC

Our SPICAV retrievals of m_i (mode 1 imaginary index) show a greater level of longitudinal variation of the unknown UV absorber than inferred from VMC (Lee *et al.*, 2015; Bertaux *et al.*, 2016); for example, Fig. 12 does not indicate that Aphrodite is a region where the cloud top albedo is uniquely bright compared to all other longitudes, unlike what is indicated by Bertaux *et al.* (2016). Similarly, the latitude variation at southern latitudes is more complex than what is seen in VMC at southern latitudes. On the other hand, the latitudinal variations inferred from the SPICAV analysis at northern latitudes shows the expected pattern of low latitudes darker than high ~~at~~ for almost all longitudes. These ~~complexities~~ complex spatial patterns are likely more readily discernible in the SPICAV data, because these data may be used to distinguish between different particle modes (effectively ~~segregating~~ distinguishing between mode 2 H_2SO_4 particles mostly conservative scatter-

ing ~~from~~ and mode 1 absorption), while VMC traces only the total absorption in the 365 nm band, thus likely to include both mode 1 and mode 2 contributions. Moreover, SPICAV reconstructed maps include long-term temporal variations due to the slow *Venus Express* orbital swath precession relative to longitude and/or local solar time, which may explain the overall larger variability seen by SPICAV compared to instantaneous VMC maps.

5.2. Requirements for deep vertical mixing

Since SO_2 transient enhancements and correlated UV brightenings are caused by local upwellings – also called "plumes" by e.g. Encrenaz *et al.* (2016)~~)~~, clues to the processes that support the observed SO_2 spatial distributions and the impact of SO_2 enhancement plumes can be derived by considering the LST, latitude and longitude patterns revealed in the statistically averaged data. As described in §4.3 and shown in Fig. 11, regions of SO_2 enhancements have been observed primarily at latitudes smaller than 30° except at *Aphrodite Terra* longitudes (60°-140°E) where the SO_2 enhancement extends to 40°S so that on average the SO_2 abundance from 0° tp 40°S is higher than observed at the same latitudes in the 160°-240°E region. Additionally, on average a very strong enhancement region is typically observed downwind from Aphrodite at 30-45°E. On the other hand, depletion of SO_2 noted between 10:00 to 14:00 local solar time (Fig. 10) implies that at these local solar times replenishment of the cloud top SO_2 abundance via large-scale mixing cannot keep up with the high rate of photochemical loss that would dominate at these local solar times at low latitude.

The prevalence of Venus' cloud top SO_2 abundance to peak at low latitudes was already noticed in our first analysis (Marcq *et al.*, 2011, 2013),

and was then linked to the general meridional circulation causing upwelling at lower latitudes and downwelling at higher latitudes. Therefore, the combined SPICAV, TEXES and HST results confirm that the mechanism driving transient plume formation differs distinctely from shallow sub-solar mixing and deep Hadley-cell circulation processes.

The observed increase in SO_2 abundance in the 0° to 40°S latitude region at longitudes intersecting *Aphrodite Terra* relative to what is observed at similar latitudes upwind provides further evidence to the unexpected connection between surface topography and cloud top (Bertaux *et al.*, 2016; Peralta *et al.*, 2017). In general, the current analysis shows that statistically on average SO_2 is high at low latitudes from 40° to 120°E relative to other longitudes except at 30°-45°E (downwind from Aphrodite) where the SO_2 abundance is on average higher than at Aphrodite. We still do not completely understand what controls the overall SO_2 longitudinal variation (provided it is genuine and not an artifact from our temporal-longitudinal sampling). Nevertheless, the relative increase in SO_2 between the region downwind of Aphrodite and directly over Aphrodite are consistent with the differences in wind speed within those two specific regions and the anticipated vertical wind speed response proposed by Bertaux *et al.* (2016), as we already suggested in §4.2.1 while discussing the possible 110-day period in SO_2. The differences in wind speed between these two regions are likely linked to the impact of gravity waves (Navarro *et al.*, 2018) momentum deposition on cloud top zonal wind speeds as proposed by Bertaux *et al.* (2016).

Interestingly, Encrenaz *et al.* (2016) does not see any SO_2 plume over this location (see Fig. 11), which highlights that while the discussed SO_2 enhance-

ment over the western slopes of *Aphrodite Terra* is on average higher than other longitude regions, other transient phenomena may also be relevant, such as local time effects shown in Fig. 13. In fact, TEXES measurements were acquired above *Aphrodite Terra* at 13:30 local time, further confirming that transient plume activity is suppressed directly over *Aphrodite* near local noon. Similarly, STIS observations from Jessup and Mills (2019) show that increased 245 nm cloud top darkening occurs over regions of low elevation 2 hours LST prior to local noon, but these increases are not observed at similar local times directly over *Aphrodite Terra*.

6. Conclusion

Our analysis of the full SPICAV-UV nadir data set has been performed by fitting the observed radiance factors with respect to SO_2 abundance at cloud top and UV absorption of mode 1 particles. Our previous conclusions about SO_2 (Marcq *et al.*, 2011, 2013) are mostly confirmed: in average, SO_2 is found to be decreasing with increasing latitude, from typically 5-100 ppbv at 70 km near the equator to 2-20 ppbv polewards of 60°N and S. Statistical dispersion is therefore much larger at lower latitudes, consistent with the location of transient SO_2 plumes as seen by other observers (Encrenaz *et al.*, 2016). The 5-fold secular decrease in equatorial SO_2 reported by Marcq *et al.* (2013) between 2007 and 2011 is now found to extend until 2015 at least, albeit with a previously unreported secondary maximum in 2009. A minimum near subsolar point is also found in average, likely caused by the locally higher photochemical depletion rate.

UV absorption (Fig. 13) displays the familiar pattern of comparatively

brighter mid-to-high latitudes compared to lower latitudes (Titov *et al.*, 2018), along with an already known darkening in the 12:00-14:00 local time range at low latitudes (Titov *et al.*, 2012). Long-term evolution of UV darkness (Fig. 7) shows at first an increase between 2006 and 2011, followed by a variable, yet in ~~avergae~~ average darker UV albedo between 2011 and 2015. Such a behavior is reminiscent of the other UV-sensitive instrument on board ~~*venus*~~ *Venus Express*, namely VMC (Lee *et al.*, 2015, 2019).

We have also investigated possible correlations with topography. Since longtudinal and temporal sampling are correlated to the slowly precessing *Venus Express* polar orbit, such correlations are hard to disentangle from temporal variability. With this *caveat* in mind, topographic signature of *Aphrodite Terra* is possibly seen both in SO_2, with high SO_2 levels reported direcly downwind of *Aphrodite Terra* in the 30°-45°E zonal region, and in UV brightness with a comparatively brighter cloud top above and downwind from *Aphrodite Terra*. Both findings are consistent with VMC studies of UV albedo (Bertaux *et al.*, 2016) and SO_2 behavior as seen by STIS/HST (Jessup *et al.*, 2015), and explained through coupled variations in vertical mixing and zonal wind speed through momentum deposition from topography-induced gravity waves over the western edge of *Aphrodite Terra*.

In any case, the high temporal and spatial variability of both SO_2 and UV absorption over a large span of temporal (from days to decades) and spatial (from regional to planetary) scales highlight the need to continue the monitoring of Venus after the end of *Venus Express*, from orbiters like *Akatsuki* and Earth-based observations, at least until the next generation of UV instruments on board Venus orbiters may take over the legacy of *Venus*

Express at some point in the late 2020s to early 2030s.

Acknowledgements

We wish to acknowledge the support of CNES and ESA for this work. As a result from this support, it is planned to deliver to ESA Planetary Science Archives (PSA) both the day side nadir UV albedo spectra and the columns of SO_2 and ozone derived from SPICAV/Venus Express mission. EM, JLB, FL and FM acknowledge support Programme National de Plantologie (AT-MARVEN grant) during this analysis. DB, OK and JLB wish to acknowledge the support of the Ministry of Education and Science of Russian Federation grant 14.W03.31.0017. KLJ acknowledges support for her contributions to this work were provided through NASA Venus Climate Orbiter, Participating Scientist Program grant number NNX16AK82G.

Arney, G., Meadows, V., Crisp, D., Schmidt, S.J., Bailey, J., Robinson, T., 2014. Spatially resolved measurements of H_2O, HCl, CO, OCS, SO_2, cloud opacity, and acid concentration in the Venus near-infrared spectral windows. Journal of Geophysical Research (Planets) 119, 1860–1891.

Barker, E.S., 1979. Detection of SO_2 in the UV spectrum of Venus. Geophys. Res. Lett. 6, 117–120.

Belyaev, D., Korablev, O., Fedorova, A., Bertaux, J., Vandaele, A., Montmessin, F., Mahieux, A., Wilquet, V., Drummond, R., 2008. First observations of SO_2 above Venus' clouds by means of Solar Occultation in the Infrared. Journal of Geophysical Research (Planets) 113, 1–10.

582 Bertaux, J.L., Khatuntsev, I.V., Hauchecorne, A., Markiewicz, W.J., Marcq,
583 E., Lebonnois, S., Patsaeva, M., Turin, A., Fedorova, A., 2016. Influence
584 of Venus topography on the zonal wind and UV albedo at cloud top level:
585 The role of stationary gravity waves. Journal of Geophysical Research
586 (Planets) 121, 1087–1101.

587 Bertaux, J.L., Nevejans, D., Korablev, O., Villard, E., Quémerais, E., Neefs,
588 E., Montmessin, F., Leblanc, F., Dubois, J.P., Dimarellis, E., Hauchecorne,
589 A., Lefèvre, F., Rannou, P., Chaufray, J.Y., Cabane, M., Cernogora, G.,
590 Souchon, G., Semelin, F., Reberac, A., van Ransbeek, E., Berkenbosch, S.,
591 Clairquin, R., Muller, C., Forget, F., Hourdin, F., Talagrand, O., Rodin,
592 A., Fedorova, A., Stepanov, A., Vinogradov, I., Kiselev, A., Kalinnikov,
593 Y., Durry, G., Sandel, B., Stern, A., Gérard, J.C., 2007. SPICAV on
594 Venus Express: Three spectrometers to study the global structure and
595 composition of the Venus atmosphere. Plan. and Space Sci. 55, 1673–1700.

596 Bézard, B., de Bergh, C., Fegley, B., Maillard, J.P., Crisp, D., Owen, T.,
597 Pollack, J.B., Grinspoon, D., 1993. The abundance of sulfur dioxide below
598 the clouds of Venus. Geophys. Res. Letters 20, 1587–1590.

599 Bohlin, R.C., Gordon, K.D., Tremblay, P.E., 2014. Techniques and review
600 of absolute flux calibration from the ultraviolet to the mid-infrared. Pub-
601 lications of the Astronomical Society of the Pacific 126, 711.

602 Dahlback, A., Stamnes, K., 1991. A new spherical model for comput-
603 ing the radiation field available for photolysis and heating at twilight.
604 Planet. Space Sci. 39, 671–683.

Encrenaz, T., Greathouse, T.K., Marcq, E., Sagawa, H., Widemann, T., Bézard, B., Fouchet, T., Lefèvre, F., Lebonnois, S., Atreya, S.K., Lee, Y.J., Giles, R., Watanabe, S., 2019. HDO and SO_2 thermal mapping on Venus. IV. Statistical analysis of the SO_2 plumes. A&A 623, A70.

Encrenaz, T., Greathouse, T.K., Richter, M.J., DeWitt, C., Widemann, T., Bézard, B., Fouchet, T., Atreya, S.K., Sagawa, H., 2016. HDO and SO_2 thermal mapping on Venus. III. Short-term and long-term variations between 2012 and 2016. A&A 595, A74.

Encrenaz, T., Greathouse, T.K., Roe, H., Richter, M., Lacy, J., Bézard, B., Fouchet, T., Widemann, T., 2012. HDO and SO_2 thermal mapping on Venus: evidence for strong SO_2 variability. A&A 543, A153.

Esposito, L.W., 1984. Sulfur dioxide - Episodic injection shows evidence for active Venus volcanism. Science 223, 1072–1074.

Esposito, L.W., Copley, M., Eckert, R., Gates, L., Stewart, A.I.F., Worden, H., 1988. Sulfur dioxide at the Venus cloud tops, 1978-1986. J. Geophys. Res. 93, 5267–5276.

Esposito, L.W., Winick, J.R., Stewart, A.I., 1979. Sulfur dioxide in the Venus atmosphere - Distribution and implications. Geophys. Res. Lett. 6, 601–604.

Frandsen, B.N., Wennberg, P.O., Kjaergaard, H.G., 2016. Identification of OSSO as a near-UV absorber in the Venusian atmosphere. Geophys. Res. Lett. 43, 11.

Haus, R., Kappel, D., Arnold, G., 2015. Radiative heating and cooling in the middle and lower atmosphere of Venus and responses to atmospheric and spectroscopic parameter variations. Planet. Space Sci. 117, 262–294.

Hummel, J.R., Shettle, E.P., Longtin, D.R., 1988. A new background stratospheric aerosol model for use in atmospheric radiation models. Technical Report. OPTIMETRICS INC BURLINGTON MA.

Ignatiev, N.I., Titov, D.V., Piccioni, G., Drossart, P., Markiewicz, W.J., Cottini, V., Roatsch, T., Almeida, M., Manoel, N., 2009. Altimetry of the Venus cloud tops from the Venus Express observations. Journal of Geophysical Research (Planets) 114, E00B43.

Jenkins, E.B., Morton, D.C., Sweigart, A.V., 1969. Rocket Spectra of Venus and Jupiter from 2000 TO 3000 Å. ApJ 157, 913.

Jessup, K.L., Marcq, E., Mills, F., Mahieux, A., Limaye, S., Wilson, C., Allen, M., Bertaux, J.L., Markiewicz, W., Roman, T., Vandaele, A.C., Wilquet, V., Yung, Y., 2015. Coordinated Hubble Space Telescope and Venus Express Observations of Venus' upper cloud deck. Icarus 258, 309–336.

Jessup, K.L., Mills, F.P., 2019. On Venus' Cloud Top Chemistry, Convective Activity and Topography: A Perspective from HST. Icarus under revision.

Lee, Y.J., Imamura, T., Schröder, S.E., Marcq, E., 2015. Long-term variations of the UV contrast on Venus observed by the Venus Monitoring Camera on board Venus Express. Icarus 253, 1–15.

649 Lee, Y.J., Jessup, K.L., Perez-Hoyos, S., Titov, D.V., Lebonnois, S., Per-
650 alta, J., Horinouchi, T., Imamura, T., Limaye, S., Marcq, E., Takagi, M.,
651 Yamazaki, A., Yamada, M., Watanabe, S., Murakami, S., Ogohara, K.,
652 McClintock, W.M., Holsclaw, G., Roman, A., 2019. Long-term variations
653 of Venus' 365-nm albedo observed by Venus Express, Akatsuki, MESSEN-
654 GER and Hubble Space Telescope. ApJ under revision.

655 Lee, Y.J., Yamazaki, A., Imamura, T., Yamada, M., Watanabe, S., Sato,
656 T.M., Ogohara, K., Hashimoto, G.L., Murakami, S., 2017. Scattering
657 Properties of the Venusian Clouds Observed by the UV Imager on board
658 Akatsuki. AJ 154, 44.

659 Luginin, M., Fedorova, A., Belyaev, D., Montmessin, F., Wilquet, V., Ko-
660 rablev, O., Bertaux, J.L., Vandaele, A.C., 2016. Aerosol properties in the
661 upper haze of Venus from SPICAV IR data. Icarus 277, 154–170.

662 Marcq, E., Baggio, L., Lefèvre, F., Stolzenbach, A., Montmessin, F., Belyaev,
663 D., Korablev, O., Bertaux, J.L., 2019. Discovery of cloud top ozone on
664 Venus. Icarus 319, 491–498.

665 Marcq, E., Belyaev, D., Montmessin, F., Fedorova, A., Bertaux, J.L., Van-
666 daele, A.C., Neefs, E., 2011. An investigation of the SO_2 content of the
667 venusian mesosphere using SPICAV-UV in nadir mode. Icarus 211, 58–69.

668 Marcq, E., Bertaux, J.L., Montmessin, F., Belyaev, D., 2013. Variations of
669 sulphur dioxide at the cloud top of Venus's dynamic atmosphere. Nature
670 Geoscience 6, 25–28.

671 Marcq, E., Bézard, B., Drossart, P., Piccioni, G., Reess, J.M., Henry, F.,
672 2008. A latitudinal survey of CO, OCS, H_2O, and SO_2 in the lower at-
673 mosphere of Venus: Spectroscopic studies using VIRTIS-H. Journal of
674 Geophysical Research (Planets) 113, 0–+.

675 Marcq, E., Mills, F.P., Parkinson, C.D., Vandaele, A.C., 2018. Composition
676 and Chemistry of the Neutral Atmosphere of Venus. Space Sci. Rev. 214,
677 #10.

678 McClintock, W.E., Rottman, G.J., Woods, T.N., 2005. Solar-Stellar Irradi-
679 ance Comparison Experiment II (SOLSTICE II): Instrument Concept and
680 Design. Springer New York, New York, NY. pp. 225–258.

681 Moroz, V.I., Zasova, L.V., 1997. VIRA-2: a review of inputs for updating the
682 Venus International Re ference Atmosphere. Advances in Space Research
683 19, 1191–1201.

684 Na, C.Y., Esposito, L.W., McClintock, W.E., Barth, C.A., 1994. Sulfur
685 dioxide in the atmosphere of Venus. 2: Modeling results. Icarus 112, 389–
686 395.

687 Navarro, T., Schubert, G., Lebonnois, S., 2018. Atmospheric mountain wave
688 generation on Venus and its influence on the solid planet's rotation rate.
689 Nature Geoscience 11, 487–491.

690 Newville, M., Stensitzki, T., Allen, D.B., Ingargiola, A., 2014. LMFIT: Non-
691 Linear Least-Square Minimization and Curve-Fitting for Python.

692 Peralta, J., Hueso, R., Sánchez-Lavega, A., 2007. Cloud brightness distri-
693 bution and turbulence in Venus using Galileo violet images. Icarus 188,
694 305–314.

695 Peralta, J., Hueso, R., Sánchez-Lavega, A., Lee, Y.J., Muñoz, A.G.,
696 Kouyama, T., Sagawa, H., Sato, T.M., Piccioni, G., Tellmann, S., Ima-
697 mura, T., Satoh, T., 2017. Stationary waves and slowly moving features in
698 the night upper clouds of Venus. Nature Astronomy 1, 0187. 1707.07796.

699 Pérez-Hoyos, S., Sánchez-Lavega, A., García-Muñoz, A., Irwin, P.G.J., Per-
700 alta, J., Holsclaw, G., McClintock, W.M., Sanz-Requena, J.F., 2018.
701 Venus Upper Clouds and the UV Absorber From MESSENGER/MASCS
702 Observations. Journal of Geophysical Research (Planets) 123, 145–162.
703 1801.03820.

704 Sander, S.P., Abbatt, J., Barker, J.R., Burkholder, J.B., Friedl, R.R.,
705 Golden, D.M., Huie, R.E., Kolb, C.E., Kurylo, M.J., Moortgat, G.K.,
706 Orkin, V.L., Wine, P.H., 2011. Chemical Kinetics and Photochemical
707 Data for Use in Atmospheric Studies, Evaluation number 17. Technical
708 Report. Jet Propulsion Laboratory.

709 Titov, D.V., Ignatiev, N.I., McGouldrick, K., Wilquet, V., Wilson, C.F.,
710 2018. Clouds and Hazes of Venus. Space Sci. Rev. 214, 126.

711 Titov, D.V., Markiewicz, W.J., Ignatiev, N.I., Song, L., Limaye, S.S.,
712 Sanchez-Lavega, A., Hesemann, J., Almeida, M., Roatsch, T., Matz, K.D.,
713 Scholten, F., Crisp, D., Esposito, L.W., Hviid, S.F., Jaumann, R., Keller,

714 H.U., Moissl, R., 2012. Morphology of the cloud tops as observed by the
715 Venus Express Monitoring Camera. Icarus 217, 682–701.

716 Titov, D.V., Taylor, F.W., Svedhem, H., Ignatiev, N.I., Markiewicz, W.J.,
717 Piccioni, G., Drossart, P., 2008. Atmospheric structure and dynamics as
718 the cause of ultraviolet markings in the clouds of Venus. Nature 456,
719 620–623.

720 Vandaele, A.C., Korablev, O., Belyaev, D., Chamberlain, S., Evdokimova,
721 D., Encrenaz, T., Esposito, L., Jessup, K.L., Lefèvre, F., Limaye, S., 2017a.
722 Sulfur dioxide in the Venus atmosphere: I. Vertical distribution and vari-
723 ability. Icarus 295, 16–33.

724 Vandaele, A.C., Korablev, O., Belyaev, D., Chamberlain, S., Evdokimova,
725 D., Encrenaz, T., Esposito, L., Jessup, K.L., Lefèvre, F., Limaye, S.,
726 Mahieux, A., Marcq, E., Mills, F.P., Montmessin, F., Parkinson, C.D.,
727 Robert, S., Roman, T., Sandor, B., Stolzenbach, A., Wilson, C., Wilquet,
728 V., 2017b. Sulfur dioxide in the Venus Atmosphere: II. Spatial and tem-
729 poral variability. Icarus 295, 1–15.

730 Zasova, L.V., Moroz, V.I., Esposito, L.W., Na, C.Y., 1993. SO_2 in the Middle
731 Atmosphere of Venus: IR Measurements from Venera-15 and Comparison
732 to UV Data. Icarus 105, 92–109.